ACS NANO

www.acsnano.org

ARTICLE

Programmable Self-Assembly of Nanoplates into Bicontinuous Nanostructures

Hideaki Tanaka, Tomonari Dotera,* and Stephen T. Hyde

Cite This: *ACS Nano* 2023, 17, 15371−15378

Read Online

ACCESS | Metrics & More | Article Recommendations | Supporting Information

ABSTRACT: **Self-assembly is the process by which individual components arrange themselves into an ordered structure by changing the shapes, components, and interactions. It has enabled us to construct an extensive range of geometric forms on many length scales. Nevertheless, the potential of two-dimensional polygonal nanoplates to self-assemble into extended three-dimensional structures with compartments and corridors has remained unexplored. In this paper, we show coarse-grained Monte Carlo simulations demonstrating self-assembly of hexagonal/triangular nanoplates via complementary interactions into faceted, sponge-like "bicontinuous polyhedra" (or infinite polyhedra) whose flat walls partition space into a pair of mutually interpenetrating labyrinths. Two bicontinuous polyhedra can be self-assembled: the regular (or Platonic) Petrie−Coxeter infinite polyhedron (denoted {6,4|4}) and the semi-regular Hart "gyrangle". The latter structure is chiral, with both left- and right-handed versions. We show that the Petrie−Coxeter assembly is constructed from two complementary populations of hexagonal nanoplates. Furthermore, we find that the 3D chiral Hart gyrangle can be assembled from identical achiral triangular nanoplates decorated with regioselective complementary interaction sites. The assembled Petrie−Coxeter and Hart polyhedra are faceted versions of two of the simplest triply periodic minimal surfaces, namely, Schwarz's primitive and Schoen's gyroid surfaces, respectively, offering alternative routes to those bicontinuous nanostructures, which are widespread in synthetic and biological materials.**

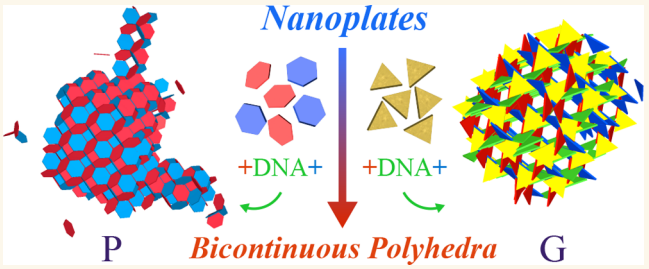

KEYWORDS: *programmable self-assembly, DNA-functionalized nanoplates, simulation of nanostructures, bicontinuous structures, gyroid, infinite polyhedra, gyrangle*

Over the past two decades, superb research fronts have emerged for self-assembly[1,2] of geometric nanoblocks: columnar assembly of colloidal polygons,[3,4] tethered nanoblocks,[5] polygonal nanoplates,[6−12] and polyhedra.[13−20] To date, several self-folding origami processes have been reported to allow the self-assembly of flat polygons into three-dimensional polyhedra.[21−24] However, the formation of extended, porous three-dimensional structures from modular components has not been achieved. A number of sophisticated three-dimensional molecular structures and devices built of DNA strands have been developed with various tools from DNA nanotechnology, such as DNA origami, DNA bricks, and wireframe DNA polyhedra.[25−28] Further, nanoparticles have been rationally assembled into macroscopic materials, where the particle interactions are tuned with DNA patches.[29−32] Similarly, regioselective and programmable surface encoding of colloidal nanoparticles decorated with single-stranded DNA has been demonstrated.[33] These principles of selective, directional interparticle interactions with DNA offer a promising path to various geometries of self-assembled materials over a range of length scales. Indeed, recent advances in the fabrication of icosahedral shells[34] or tubules[35,36] with positive or negative curvatures respectively from programmable triangular building blocks constructed from DNA origami confirm the efficiency of this approach. Here we harness those concepts and propose explicit recipes for the construction of nanoscaled bicontinuous polyhedra from polygonal (hexagonal and triangular) nanoplates, assembled via regioselective interactions between programmable, complementary, DNA strands,[37] frames,[38] or surface ligands[16] decorating plate edges.

RESULTS

Infinite Polyhedra. "Regular infinite polyhedra" were discovered a century ago by Petrie and Coxeter, reported later

Received: November 30, 2022
Accepted: July 14, 2023
Published: August 1, 2023

by Coxeter.[39] They are natural extensions of the well-known Platonic polyhedra, since they too have symmetrically identical faces, edges, and vertices (and are characterized by a single "flag"[40]). There are three regular infinite polyhedra: {6,4|4}, {4,6|4}, and {6,6|3}, where the notation {*p*,*q*|*r*} implies a polyhedron, at whose vertex *q* of regular *p*-gons meet, and which has *r*-gonal holes.[39] Their Platonic nature is useful in our context since the geometric equivalence of all polygonal faces and vertices reduces the variety of interparticle interactions needed to guide their assembly.

One of our target patterns is the regular {6,4|4} infinite polyhedron shown in Figure 1a, which we refer to here as the

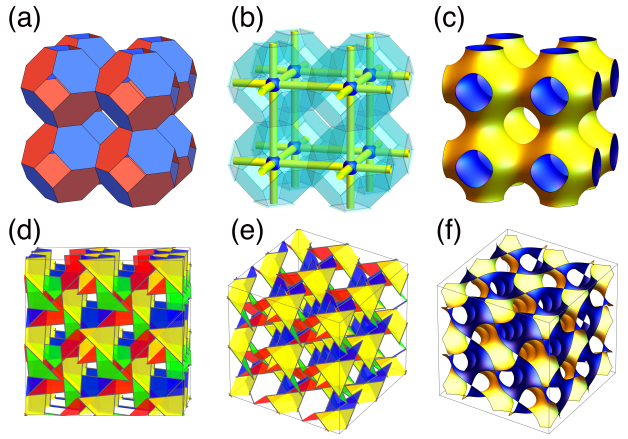

Figure 1. Infinite bicontinuous polyhedra. (a) {6,4|4} regular infinite polyhedron (with space group $Im\bar{3}m$) composed of truncated octahedra. (b) Jungle-gym labyrinth threading one side of the sponge structure. (c) The triply periodic primitive surface, associated with the {6,4|4} infinite polyhedron. (d, e) Two views of a "gyrangle", another regular infinite polyhedron (with space group $I4_132$). The gyrangle consists of four sets of (like-colored) parallel triangles normal to the body diagonals of the cubic unit cell. (f) The triply periodic gyroid surface (space group $Ia\bar{3}d$) viewed from the same direction as the gyrangle in (e).

"truncated octahedral sponge" since its cubic unit cell contains a single truncated octahedron, consisting of eight (equilateral) hexagons facing the {111} directions of the cube. The infinite polyhedron results by appending copies of that cell in all three lattice directions, resulting in an extended sponge (space group $Im\bar{3}m$) built of a single faceted sheet tiled by flat hexagons with four hexagons surrounding each vertex. The resulting convoluted sheet divides space into two identical, infinite jungle-gym labyrinths (Figure 1b), which thread each other just as in the triply periodic minimal surface known as the Schwarz Primitive surface,[41,42] displayed in Figure 1c.

Our second target structure is shown in Figures 1d and 1e: an infinite plane-faced polyhedron composed of equilateral triangles, topologically equivalent to another well-known triply periodic minimal surface, the gyroid (Figure 1f).[43−49] That pattern, the "gyrangle", discovered by Hart around 1980, is more elusive.[50] It has remained relatively unknown until its more recent dissemination within mathematical and scientific circles.[51] Four equilateral triangles meet at every vertex of the gyrangle; however, two of those triangles are offset by a *half-edge* as shown in Figure 2a, so that each triangle includes six vertices, located on its corners and mid-edges. The resulting infinite polyhedron can also be described as Platonic, since all faces, edges, and vertices are symmetrically equivalent. (More technically, it is semi-regular, or "chiral" in a different sense to geometrical chirality, with a pair of flags.[40])

The same structure emerged recently as an optimal embedding in three-space of the regular hyperbolic triangulation 3^8, with eight equilateral triangles around each vertex[48] as shown in Figure 2b. If all pairs of nearest vertices on the equilateral triangular facet of the gyrangle are joined by a straight edge, then the facet is dissected into four smaller equilateral triangles. Vertices located midway on an edge of the triangular facet are common to three adjacent smaller triangles (3^3), while those on the corners include just one (3^1). Each facet vertex is common to four adjacent facets, so that each vertex has the symbol $3^1.3^3.3^1.3^3$ (i.e., 3^8), from which perspective we rediscovered the "gyrangle" regular infinite polyhedron. A three-dimensional visual presentation of the gyrangle in terms of the regular hyperbolic triangulation 3^8 is provided in Supporting Movie S1. We ignore those smaller equilateral triangles within the gyrangle and consider only their 4-fold unions, the larger triangular facets.

The module displayed in Figure 2c is composed of eight triangles split into four pairs of parallel triangles. Each parallel pair is formed by rotating one of two overlapping triangles by 180° along a shared edge and translating along an axis normal to that edge. With one pair in place, the remaining three are positioned to induce dihedral 3-fold point symmetry D_3. The resulting element has two chiralities, as shown in Figure 2d; the gyrangle is therefore geometrically chiral. Either enantiomer is arranged in a body-centered cubic (bcc) Bravais lattice as in Figure 2e, whose unit cell contains 16 equilateral triangles, with gaps. Adjoining unit cells fill those gaps so that every vertex is occupied by four triangles. The normals to all triangles in the gyrangle point along tetrahedral directions, i.e., (111), ($\bar{1}$11), (1$\bar{1}$1), and (11$\bar{1}$).

The gyroid minimal surface is geometrically achiral, as it divides space into a pair of equal-volume left- and right-handed labyrinths related by inversion symmetry (Figure 2f). Each labyrinth is threaded by a single Laves' *srs* net, known to Wells as the (10,3)-a net.[52] Edges of the *srs* nets wind around (111) directions, forming 3-fold helices, and (100) directions, forming tighter 4-fold helices, as shown in Figure 2h. (Note that the helical character of the *srs* net is nicely illustrated in Wells' book.[52]) Similarly, the gyrangle forms a pair of chiral *srs* labyrinths (Figure 2g). However, in contrast to the gyroid, one labyrinth is more voluminous than the other; consequently, the space group is chiral, with space group $I4_132$ (No. 214, or 246 orbifold), as found in ABC block copolymers[44] and in butterfly wings.[47] The Wyckoff positions of the gyrangle vertices within that group are described in the Methods section.

We find it helpful to refer to these infinite polyhedra as "bicontinuous polyhedra" in the context of self-assembly, capturing both their infinite and bicontinuous natures.

Models for Self-Assembly. We propose that the specific self-assemblies of nanoscale hexagonal and triangular plates can be directed via complementary DNA sequences tethered to the facets' edges, as illustrated in Figure 3a. To explore that idea, we model these composite plates as rigid polygonal discs, decorated by patch particles located on their edges, displayed in Figure 3b,g. We design the complementary interactions to disfavor simpler flat structures, 6^3 (Figure 3c) and 3^6 (Figure 3h), favoring instead faceted sheets with negative Gaussian curvature, characteristic of bicontinuous polyhedra. Complementary (effectively attractive) interactions are modeled by charging the patchy particles, coloring them as (positively charged) red or (negatively charged) blue particles, whose mutual interactions

https://doi.org/10.1021/acsnano.2c11929
ACS Nano 2023, 17, 15371−15378

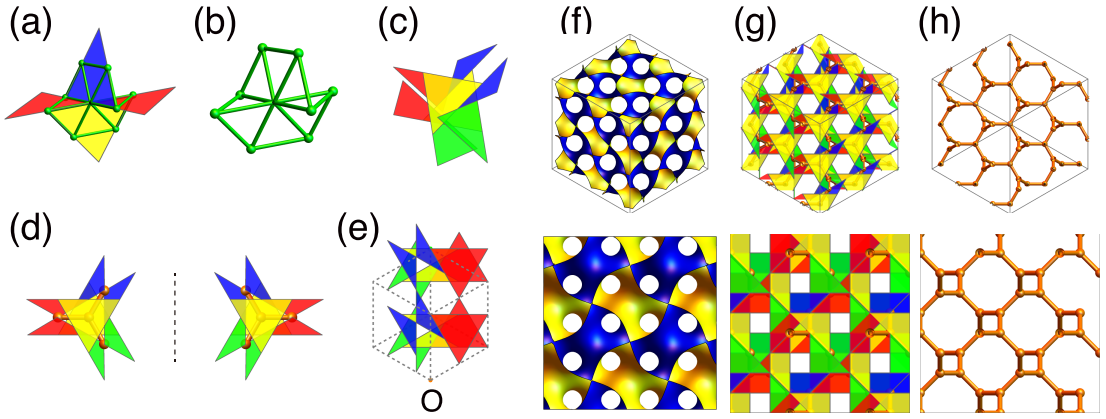

Figure 2. Schematic of the geometry of a gyrangle. (a) Four equilateral triangles meet at a vertex joined half-edge to half-edge. (b) Corresponding $3^1.3^3.3^1.3^3$ (i.e., 3^8) vertex obtained from the regular hyperbolic triangulation. We ignore vertices located midway on an edge of triangles and smaller equilateral triangles within the gyrangle. (c) A chiral structural element consisting of 8 triangles with D_3 point symmetry, containing four pairs of (like-colored) parallel triangles. Parallel triangles are rotated by 180° with respect to each other. (d) A chiral pair of structural elements related by a mirror located on the vertical dashed line. The orange Y-shaped network, sandwiched between a pair of (yellow) parallel triangles, forms a fragment of the triply periodic chiral *srs* network. Either chiral element forms a (left- or right-handed) gyrangle. (e) A body-centered cubic unit cell of the gyrangle, with 16 triangles. (f) [111] and [100] views of gyroid surfaces (space group $Ia\bar{3}d$). (g) Corresponding gyrangle superimposed by orange points centered between two parallel triangles, forming an *srs* network (space group $I4_132$). One labyrinth is more voluminous than the other; consequently, the number of visible hexagonal/square holes is half that of the circular holes in the [111]/[100] views of the gyroid. (h) A single *srs* network (which threads one side of the gyroid).

are attractive if interacting particles have opposite signs, or repulsive otherwise. Thus, red and blue particles model interactions between complementary single-stranded DNA, which have been demonstrated in recent technologies.[37,38]

The nanoscale plates are studded with gray particles, indicating the position of nodes, and with colored patchy particles around their edges.[14,15] As shown in Figure 4a−e, each plate edge is decorated with two rows of 11 nodes, in the case of the hexagonal plates, and two rows of 12 (Model I) and 16 (Model II) nodes for triangular plates. Thus, the thickness σ of the hard nanoplates is $\sigma = l/10$, and $\sigma = l/11$ and $\sigma = l/15$ for hexagons and triangles, respectively, where l is the edge length of the polygons. We note that these designs lead to ideal packing (volume) fractions of nanoplates in the ideal solidified self-assemblies of ca. 0.085, and 0.155 and 0.126 for the {6,4|4} and the gyrangle (Models I and II), respectively, as described in detail in the Methods section. Actual packing fractions are much less than the ideal values because of open spaces of simulation boxes (corresponding to solvent): 0.017 and 0.038/0.028. The centers of gray nodes contribute to hard-core steric interactions only. Colored particles mutually interact more strongly, as outlined below. The designs of colored patches on nanoplate edges have been chosen to favor the arrangements of adjacent plates in these bicontinuous polyhedra and disfavor alternative assemblies. Since adjacent faces of the {6,4|4} polyhedron have obtuse dihedral angles of (109.5°; $\cos\theta = -1/3$), sticky edges have been designed to induce that obtuse angle between adjacent hexagonal nanoplates. In the case of the gyrangle, both acute (70.5°; $\cos\theta = 1/3$) and obtuse (109.5°) angles are present, as illustrated in Figure 4f−h, constraining the designs of sticky patches bounding triangular nanoplates. To inhibit free rotations of adjacent hexagonal or triangular plates after attachment, at least two or four colored particles decorate each edge, respectively (Figure 4b,d,e). Hexagons are single-colored (either red or blue) and are decorated by a pair of like-colored particles on each edge (Figure 4b), while the regioselective triangles have red particles in the center and blue particles at both ends of each side (Figure 4d,e). We explore two alternative designs for triangular plates. The first design (Model I) includes a pair of red charges displaced toward the top and bottom faces of the plate, inducing a chiral triangle, as shown in Figure 4d. The second design (Model II) is achiral, with all patches located midway between the top and bottom faces. In that model, the patches protrude a distance of 0.6σ beyond the triangles' edges, as shown in Figure 4e; technically, the number of colored patches is doubled.

To avoid collisions between hard nanoplates, we ensured that the centers of all particles lie outside the nanoplate volumes. Note that interactions between like-colored hexagons and regions on triangles with like colors are strongly repulsive (hard contact). The interaction between colored particles whose centers are separated by distance r is described by

$$U(r) = \begin{cases} -\varepsilon & (r < \sigma;\ \gamma \neq \delta) \\ \infty & (r < \sigma;\ \gamma = \delta) \\ 0 & (r \geq \sigma) \end{cases}$$

where $\varepsilon > 0$, and γ or δ stands for red or blue. Thus far, the model potential is rather generic. To mimic single-stranded DNA, an additional requirement is needed: the closest patch to the cell can be attractive. A pair of red and blue patches act as a key and a lock, and other incoming patches are repulsive. This requirement also suppresses three or more polygons meeting at a common edge.

We note that the range of attraction for both hexagonal and triangular nanoplates is tuned to be less than the thickness of the plates (σ), to prevent columnar stacking, shown in Figure 3d. Some sterically allowed configurations of assembled hexagonal nanoplates are shown in Figure 3e. Those geometries are metastable at best and disfavored by the interactions listed above. The most likely configuration of hexagonal plates at low temperatures consists of four hexagons surrounding each vertex, resulting in one of our target assemblies, the {6,4|4} bicontinuous polyhedron shown in Figure 3f. Due to the

https://doi.org/10.1021/acsnano.2c11929
ACS Nano 2023, 17, 15371−15378

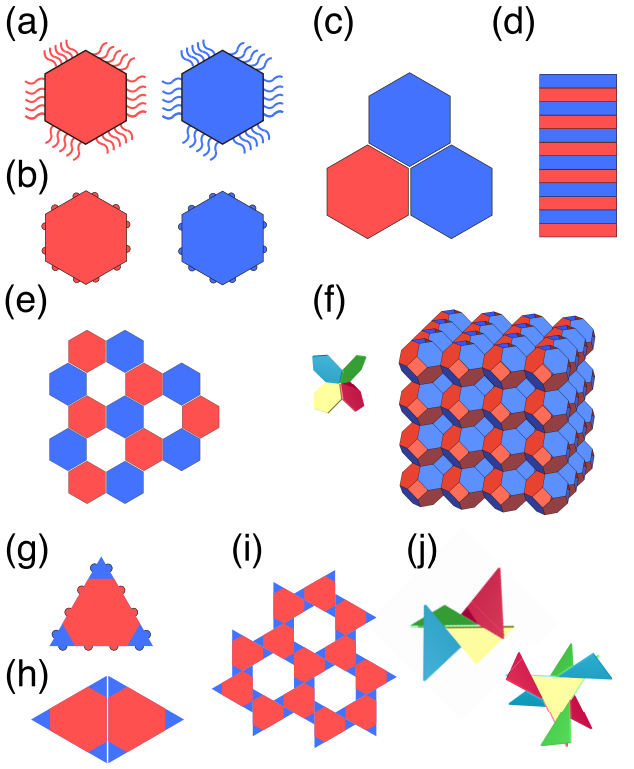

Figure 3. Model structures. (a) Schematic of a pair of hexagonal nanoplates with attached complementary (red and blue) single-stranded DNA or surface ligands. (b) Coarse-grained model hexagonal plate whose edges are decorated with patches. (c) Potential, though disfavored, planar 2D honeycomb configuration, 6^3. (d) Potential columnar configuration ($e = 0$). (e) Potential planar hexagonal configuration ($e = -3\varepsilon$). (f) The target hexagonal nanoplate assembly: a truncated octahedral sponge building the Petrie−Coxeter infinite (or bicontinuous) polyhedron {6,4|4} ($e = -6\varepsilon$). (g) Coarse-grained model of the triangular nanoplate with patches: a single two-colored triangular nanoplate, whose complementary DNA strands on the same edge are modeled by particles located in regions of different colors. (h) Potential planar triangular configuration 3^6. (i) Potential planar chiral hexagonal configuration ($e = -3\varepsilon$). (j) The target gyrangle nanoplate assembly ($e = -6\varepsilon$).

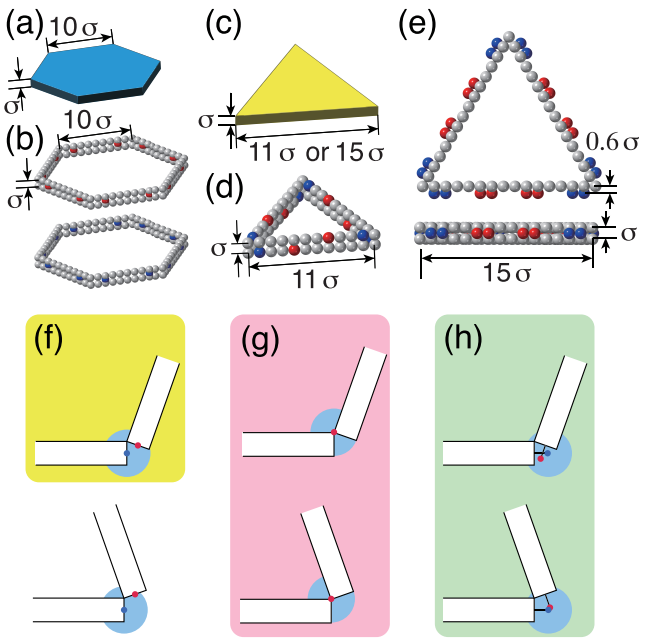

Figure 4. (a−e) Models for polygonal nanoplates bounded by nodes represented by uncharged gray balls with sticky patches composed of oppositely charged red and blue particles. (a) Hexagonal nanoplate design. (b) Our model of the boundary edges comprised 20 × 6 nodes including red/blue patch particles. (c) Triangular nanoplate design. (d) One design of triangular boundary edges (Model I), made of 22 × 3 nodes, containing built-in chiral patches. (e) An alternative edge model (Model II), with 30 × 3 nodes including protruding achiral patches. (f−h) Cross sections of targeted plate junction designs, with obtuse (109.5°) and acute (70.5°) dihedral angles between plates. Red and blue points indicate the centers of the patch particles; light blue circles indicate the interaction range of blue patches. (f) Obtuse/acute (top/bottom) geometries for hexagonal nanoplates, whose sticky patches favor the formation of the obtuse over the acute fold. (g) Triangular chiral plate junctions (Model I), for which obtuse and acute folds are equally likely. (h) Junction design for achiral triangular plates (Model II) with protruding patch particles allowing both folds.

regioselective interactions of the triangular nanoplates, the flat chiral structure shown in Figure 3i is possible. However, that pattern too is less stable than the folded arrangement of triangles characteristic of the target gyrangle polyhedron, shown in Figure 3j. Indeed, flat structures appear only transiently during the simulations, whose details are described in the Methods section.

Simulation Results. The genesis of the {6,4|4} bicontinuous polyhedron is shown in Figure 5a−f (see also Supporting Movie S2). Initially, the hexagonal plates flutter like butterflies, while embryonic assemblies with a few hexagons form and then disassemble. Later, discrete truncated octahedra composed of eight hexagons form, which nucleate further growth via the self-assembly of those truncated octahedra. Hexagons attach to the growing surface one-by-one, gradually building a bicontinuous polyhedron. The figure shows the growth of a single polyhedron, whose truncated octahedra share the same orientation as shown in Figure 5f. In this case, the simulation includes equal numbers of red and blue nanoplates to maximize the assembly efficiency. We have also conducted further simulations with unequal populations of plates, namely, $(\phi_{Red}, \phi_{Blue}) = (0.4, 0.6)$, (0.3, 0.7), (0.2, 0.8), and (0.1, 0.9) (Supporting Information SI1). In those cases, too, the same {6,4|4} polyhedron results, with no other structures, although the simulation time (in terms of Monte Carlo steps) is longer. Either scenario is feasible experimentally, and we expect that in a real experiment, after a one-pot synthesis of the self-assembled bicontinuous polyhedron, residue disaggregated nanoplates can be washed off with solvent.

Similarly, simulations of the self-assembly of triangular nanoplates decorated as per Model I give the gyrangle, as illustrated in Figure 5g−l (Supporting Movie S3; Supporting Movies S4 and S5 also show the growth of the gyrangle for achiral Model II).

During all simulations, the energy decreased, tending to a theoretical minimum of −6 per hexagonal or triangular nanoplate, realized by an infinitely extended truncated octahedral sponge or gyrangle. In practice, the energy was somewhat higher due to the finite assemblies and their accompanying surface energies. Figure 6a shows a single domain formed by a truncated octahedral sponge quenched at the reduced inverse temperature $\beta = \varepsilon/k_BT = 6.4$ and subsequently annealed at $\beta = 6.0$ and 5.8. Figures 6b and 6c present the growth of gyrangle polyhedra at $\beta = 5.4$ (chiral Model I) and $\beta = 6.4$

https://doi.org/10.1021/acsnano.2c11929
ACS Nano 2023, 17, 15371−15378

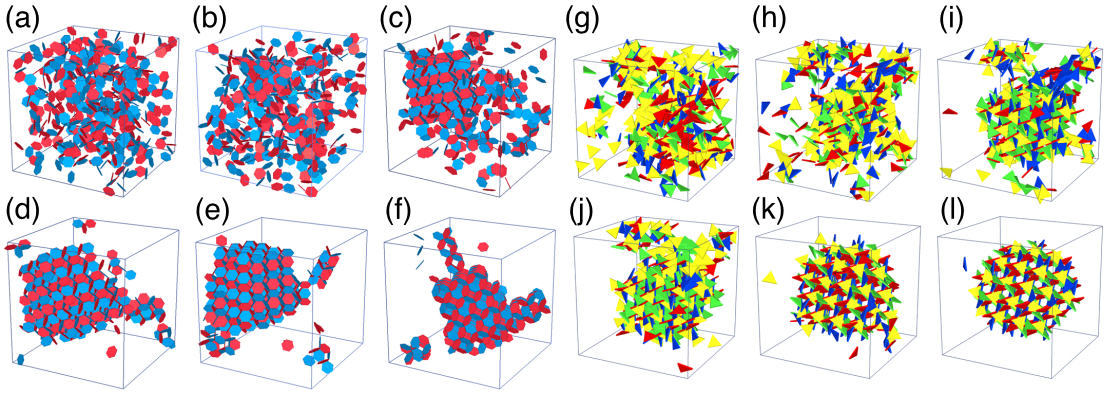

Figure 5. Growth of the truncated octahedral sponge and the gyrangle (chiral Model I) assemblies. Facets are shaded according to their unoriented normals (two colors) or oriented normals (four colors) for (a–f) and (g–l), respectively. Snapshots from simulations showing growth: (a, g) 5×10^6. (b, h) 2.5×10^7. (c, i) 5×10^7. (d, j) 10^8. (e, k) 2×10^8. (f, l) 4×10^8 Monte Carlo steps (MCS).

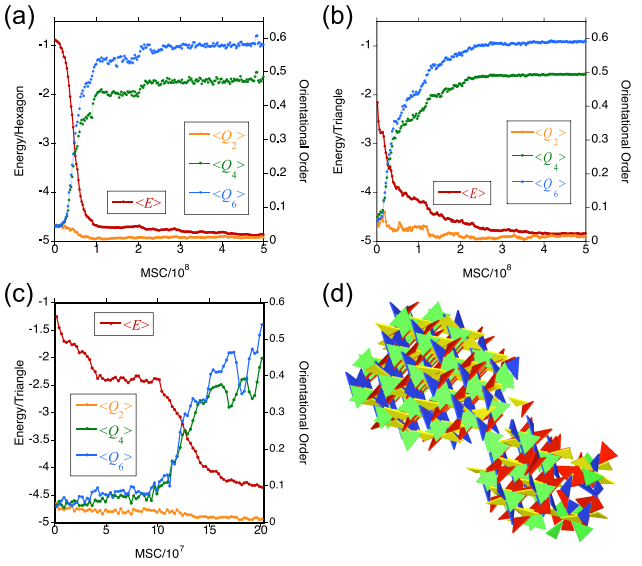

Figure 6. Energy and orientational order parameters of the truncated octahedral sponge and the gyrangle. Energy per polygon in units of ε, and orientational order parameters Q_2, Q_4, and Q_6 for normal vectors of polygons versus Monte Carlo steps are shown. (a) Growth of a truncated octahedral sponge quenched at $\beta = 6.4$ and annealed at $\beta = 6.0$ and $\beta = 5.8$. (b) Growth of a gyrangle quenched at $\beta = 5.4$ (chiral Model I). (c) Growth of a gyrangle quenched at $\beta = 6.4$ (achiral Model II). (d) Coexistence of enantiomers. Facets are shaded as in Figure 5.

(achiral Model II). The evolution of orientational order parameters[53] (defined in the Methods section) is also shown. These orientational order parameters tend to values $Q_2 = 0.000$, $Q_4 = 0.509$, and $Q_6 = 0.629$ for ideal polyhedra. For achiral model II, the coexistence of enantiomers is observed as displayed in Figure 6d.

DISCUSSION

The model assumes ideal, monodisperse, regular polygonal plates, which may be difficult to synthesize in the laboratory. In practice, systematic variations of nanoplate geometries have been observed, with plates subject to faceting, pinching, elongation, and truncation.[8] In this context, we note that truncated triangular nanoplates are also realizable in practice, forming irregular hexagons with alternating edge lengths. Those plates also assemble into bicontinuous P-like polyhedra, albeit unbalanced, with unequal volumes on either side (as in the gyrangle). The resulting convoluted sheet has space group $Pm\bar{3}m$ (a subgroup of $Im\bar{3}m$). Less regular shape fluctuations are expected to give rise to structural imperfections, such as point defects (vacancies), leading to self-limited dimensions.[35,36] However, since the system is three-dimensional, we expect that such positional and/or orientational (thermal or quenched) fluctuations are suppressed compared with those in low-dimensional systems, where positional fluctuations diverge. Rather we suspect that soft (rather than rigid) interactions may compensate for the propagation of order, even with such shape variations. A more detailed analysis of admissible variations of nanoplate geometries remains unanswered in the present study.

The geometric complexity of the targeted gyrangle assembly is relatively complex with specific dihedral angles between adjacent triangular plates. It turns out, however, that complex, direction-dependent interactions between are unnecessary, as they emerge as a result of favored edge interactions for both Models I and II. To be precise, further geometric consideration sheds light on the design principle of interactions. In the case of the hexagonal plates (Figure 4f), we can safely make the interaction range a little smaller than the thickness of the plate to prevent the columnar configuration (Figure 3d).

In the case of the targeted gyrangle, the situation is more complicated than we expected. In Model I (Figure 4g), the interaction range may be reduced to as small a value as possible. However, in Model II (Figure 4h), simulations reveal that gyrangle assembly is favored when the interacting-colored particles protrude $0.5–0.6\sigma$ beyond the triangular plate (Supporting Information SI2). Finally, we note that the half-shifted equilateral triangles spontaneously self-assemble into a right- or left-handed gyroidal Platonic solid without gaps or structural degrees of freedom with space group $I4_132$. The chirality of the resulting gyrangle is predetermined in Model I, since the triangular plates have a fixed chirality. Model II affords insights in the nucleation and growth processes of the chiral assembly, since either enantiomer is equally likely theoretically. As shown in Figure 6c, we always observed a plateau in energy at the early stage of Monte Carlo simulation due to slow nucleation. Simulations within that model, with up to 384 nanoplates, led to the growth of a single-handed giant crystal, which swallowed small embryos in our simulations (Supporting Movie S4). However, we found a preliminary simulation with 512 nanoplates showing the coexistence of enantiomers

https://doi.org/10.1021/acsnano.2c11929
ACS Nano 2023, 17, 15371–15378

(Figures 6c and 6d, Supporting Movie S5) with a long tail in energy within the simulation time. Since a gyrangle crystallite is rigid and melts from its surface only, like peeling an onion, the coarsening process cannot be due to coalescence of liquid droplets or usual crystallites. It is therefore expected that either one of two crystallites of equal size melts after a long time, or both remain, as observed in the gyroid-like assemblies of chitin found in wing scales of butterflies.[47] The details of growth of a single gyrangle enantiomer remain open along with possible applications of these self-assemblies.

CONCLUSIONS

In conclusion, we have demonstrated through Monte Carlo simulations that hexagonal/triangular nanoplates self-assemble into faceted, sponge-like bicontinuous polyhedra with compartments and corridors via complementary interactions. We have also proposed explicit recipes for constructing bicontinuous polyhedra using hexagonal and triangular nanoplates, which are assembled through regioselective interactions on the plate edges. Our focus was on two simple bicontinuous polyhedra: the well-known Petrie−Coxeter infinite polyhedron and the unsung "gyrangle". Notably, the latter structure exhibits chirality with both left- and right-handed versions. We discovered that the 3D chiral Hart gyrangle can be assembled from both chiral and achiral triangular nanoplates adorned with different junction designs. The abundance of closely related patterns in synthetic and living materials suggests that these programmable assemblies of nanoplates into primitive and gyroid-like bicontinuous structures offer valuable insights into the study of self-assembly.

METHODS

Crystallographic Description. Wyckoff positions of the gyrangle infinite polyhedron displayed in Figure 2 are as follows: Vertices of equilateral triangles are located at sites 24h (..2) of $I4_132$ with $y = 3/8$, centers of triangles are at sites 16e (.3.) with $x = 7/24$, and centers of the two parallel triangles are at sites 8b (.32), forming the *srs* network (Figure 2h). It is interesting to note that vertex locations of either hand of the gyrangle are identical, but the mutual arrangement of triangles differs.

Packing Fraction. The side of a hexagonal plate is $\sqrt{2}/4$ (= 0.354) in units of the cubic unit cell, and the total area of a sheet composed of eight hexagonal plates is $3\sqrt{3}/2$ (= 2.589). Thus, the packing fraction is $(3\sqrt{6}/8)p$ (= 0.919p), where p (= σ/l) is the ratio of the thickness to the side, ignoring the overlaps of adjacent nanoplates. In the same manner, the side of a triangular plate is $\sqrt{2}/2$ (= 0.707), and the total area of a sheet consisting of 16 triangular plates is $2\sqrt{3}$ (= 3.464). The packing fraction is $\sqrt{6}p$ (= 2.449p). For equal p, the gyrangle structure is denser than the {6,4|4} sponge because the surfaces of the gyrangle are more folded with both mountain and valley folds. For simulations, the fractions are calculated by substituting p = 1/10, 1/11, and 1/15, respectively. Since the overlaps are neglected in the above equations, the actual packing fractions are smaller. Actual fractions, including overlaps, depend on the junction design. In Figure 7, tentative curves of upper bounds (full overlaps forming a connected sheet) and lower bounds (no overlaps by self-assemblies of hexagonal prisms/truncated triangular pyramids) are shown. The lower bound for the gyrangle decreases rapidly due to the complexity of the mountain and valley folds. The values in the main text are the lower bounds. For the gyrangle structure, the volume fractions of the two labyrinths are unequal, as shown in Figure 8, as a function of the thickness of the plate using the upper-bound model. Details of calculated models are given in Supporting Information SI3.

Monte Carlo Simulations. We ran *NVT* Monte Carlo simulations confined to a cubic box under periodic boundary conditions. All runs with hexagons included N = 512 nanoplates, whereas N = 512 and N =

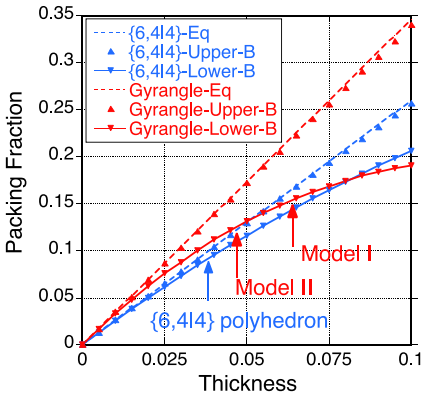

Figure 7. Packing fractions of nanoplates as functions of thickness in units of the cubic unit cell for the {6,4|4} and the gyrangle. The estimates due to the equations in the text (Eq), full overlaps (Upper Bounds), and no overlaps (Lower Bounds) are plotted.

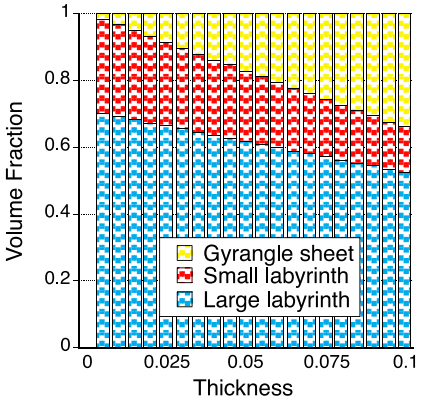

Figure 8. Volume fractions of two labyrinths as functions of thickness in units of the cubic unit cell for the gyrangle. The volumes of small and large labyrinths are deduced from the upper-bound model.

384 triangular plates were included for Models I and II, respectively. Since our goal here is to explore the most general organizational principles, independent of chemical details, we have ignored detailed solvent effects, fluid dynamics, and specific chemical interactions. In practice, we select a random plate, then translate and rotate it randomly, with respect to an arbitrary axis using quaternions. To satisfy hard steric conditions, we check all nodes on the edges of both moved and neighboring plates are outside other plates. Jump distances and rotation angles for the Monte Carlo procedures are adjusted automatically to set the acceptance ratios 1/3. No collisions and entanglements have been observed. Those stochastic movements afford an approximation of the general features of solvent immersion. The plates assemble in a heat bath, although the process is nonequilibrium. We assume that interactions between plates stemming from DNA-mediated interactions are reversible.[30,31] Starting from a random state, the simulations consist of a quenching stage at a reduced inverse temperature $\beta = \varepsilon/k_BT$ = 6.4 until 2.5×10^8 Monte Carlo steps (MCS) and annealing stages at β = 6.0 ($(2.5–4.0) \times 10^8$ MCS) and finally at β = 5.8 after 4.0×10^8 MCS for hexagonal plates to avoid metastable states and allow slow annealing. For triangular plates, we perform constant-temperature simulations at reduced inverse temperatures β = 5.4 and β = 6.4 for Models I and II, respectively. The typical number of steps was between 2 and 5×10^8 as appropriate, with similar durations of the two stages, where energy and other quantities are averaged over 2.5×10^6 MCS. Several random seeds are prepared at the same temperatures to check the dependence of the assembly process on starting configurations: the process is reproducible regardless of its initial state.

https://doi.org/10.1021/acsnano.2c11929
ACS Nano 2023, 17, 15371−15378

Orientational Order. To explore the orientational ordering of polygonal plates, we define a normal vector for the *i*th polygonal plate as $\boldsymbol{n}_i$ and evaluate $\tilde{Y}_{l,m}(\boldsymbol{n}_i)$, where $\tilde{Y}_{l,m}(\boldsymbol{n}_i)$ is a real form of spherical harmonics. The average over all plates is taken as $\tilde{Y}_{l,m} \equiv \frac{1}{N}\sum_{i=1}^{N} \tilde{Y}_{l,m}(\boldsymbol{n}_i)$. We then define the orientational order parameters that are invariant under rotations:

$$Q_l = \left(\frac{4\pi}{2l+1} \sum_{m=-l}^{l} |\tilde{Y}_{l,m}|^2 \right)^{1/2}$$

As shown in Figure 1, the octahedral sponge consists of four sets of parallel hexagons normal to the body diagonals of the cubic unit cell. Similarly, the gyrangle consists of four sets of parallel triangles normal to the body diagonals of the cubic unit cell. Accordingly, they have the same ideal Q values: $\langle Q_2 \rangle$, $\langle Q_4 \rangle$, and $\langle Q_6 \rangle$ are tending to ideal values: $Q_2 = 0.000$, $Q_4 = 0.509$, and $Q_6 = 0.629$, as shown in Figure 5.

ASSOCIATED CONTENT

Data Availability Statement

The data that support the findings of this paper and the code used to generate it are available from the corresponding author on reasonable request.

Supporting Information

The Supporting Information is available free of charge at https://pubs.acs.org/doi/10.1021/acsnano.2c11929.

SI1: self-assembly of octahedral sponge from unequal populations of plates; SI2: dependence on the distance of protruding particles in achiral Model II; SI3: pictures describing models for evaluating packing fractions (PDF)
Supporting Movie S1: Animation showing the gyrangle in terms of the regular hyperbolic triangulation 3^8 and the *srs* network (MOV)
Supporting Movie S2: Animation showing the growth of a {6,4|4} bicontinuous (infinite) polyhedron (MP4)
Supporting Movie S3: Animation showing the growth of the gyrangle (chiral Model I) (MP4)
Supporting Movie S4: Animation showing the growth of the gyrangle (achiral Model II) (MP4)
Supporting Movie S5: Animation showing the coexistence of enantiomers for the gyrangle (achiral Model II) (MP4)

AUTHOR INFORMATION

Corresponding Author

Tomonari Dotera − *Department of Physics, Kindai University, Higashiosaka City, Osaka 577-8502, Japan;* orcid.org/0000-0001-9384-0399; Email: dotera@phys.kindai.ac.jp

Authors

Hideaki Tanaka − *Department of Physics, Kindai University, Higashiosaka City, Osaka 577-8502, Japan;* orcid.org/0000-0002-1817-2850

Stephen T. Hyde − *School of Chemistry, The University of Sydney, Sydney, NSW 2006, Australia; Research School of Physics, Australian National University, Canberra, ACT 2601, Australia*

Complete contact information is available at: https://pubs.acs.org/10.1021/acsnano.2c11929

Author Contributions

H.T. and T.D. conceived the project of infinite polyhedra and performed simulations. T.D. and S.H. constructed the theoretical model of the gyrangle and wrote the manuscript.

Notes

The authors declare no competing financial interest.

ACKNOWLEDGMENTS

We thank Vanessa Robins for helpful information. This project was supported by Japan Society for the Promotion of Science through Grant-in-Aid for Scientific (B) (No. 16H04037).

REFERENCES

(1) Whitesides, G. M.; Grzybowski, B. Self-Assembly at All Scales. *Science* **2002**, *295*, 2418−2421.
(2) Ekblaw, A.; Paradiso, J.TESSERAE: Self-Assembling Shell Structures for Space Exploration. In *Proceedings of the Annual Symposium of the International Association of Shell and Spatial Structures: Extra Planetary Architecture*; IEEE, 2018; p 317.
(3) Zhang, H. T.; Wu, G.; Chen, X. H. Large-Scale Synthesis and Self-Assembly of Monodisperse Hexagon Cu_2S nanoplates. *Langmuir* **2005**, *21*, 4281−4282.
(4) Saunders, A. E.; Ghezelbash, A.; Smilgies, D. M.; Sigman, M. B., Jr.; Korgel, B. A. Columnar Self-Assembly of Colloidal Nanodisks. *Nano Lett.* **2006**, *6*, 2959−2963.
(5) Zhang, Z.; Horsch, M. A.; Lamm, M. H.; Glotzer, S. C. Tethered Nano Building Blocks: Toward a Conceptual Framework for Nanoparticle Self-Assembly. *Nano Lett.* **2003**, *3*, 1341−1346.
(6) Bowden, N.; Choi, I. S.; Grzybowski, B. A.; Whitesides, G. M. Mesoscale Self-Assembly of Hexagonal Plates Using Lateral Capillary Forces: Synthesis Using the "Capillary Bond. *J. Am. Chem. Soc.* **1999**, *121*, 5373−5391.
(7) Lapointe, C. P.; Mason, T. G.; Smalyukh, I. I. Shape-Controlled Colloidal Interactions in Nematic Liquid Crystals. *Science* **2009**, *326*, 1083−1086.
(8) Millan, J. A.; Ortiz, D.; Glotzer, S. C. Effect of Shape on the Self-Assembly of Faceted Patchy Nanoplates with Irregular Shape into Tiling Patterns. *Soft Matter* **2015**, *11*, 1386−1396.
(9) Gantapara, A. P.; Qi, W.; Dijkstra, M. A Novel Chiral Phase of Achiral Hard Triangles and an Entropy-Driven Demixing of Enantiomers. *Soft Matter* **2015**, *11*, 8684−8691.
(10) Ou, Z.; Wang, Z.; Luo, B.; Luijten, E.; Chen, Q. Kinetic Pathways of Crystallization at the Nanoscale. *Nat. Mater.* **2020**, *19*, 450−455.
(11) Fang, W.; Jia, S.; Chao, J.; Wang, L.; Duan, X.; Liu, H.; Li, Q.; Zuo, X.; Wang, L.; Wang, L.; Liu, N.; Fan, C. Quantizing Single-Molecule Surface-Enhanced Raman Scattering with DNA Origami Metamolecules. *Sci. Adv.* **2019**, *5*, No. eaau4506.
(12) Szustakiewicz, P.; González-Rubio, G.; Scarabelli, L.; Lewandowski, W. Robust Synthesis of Gold Nanotriangles and their Self-Assembly into Vertical Arrays. *ChemistryOpen* **2019**, *8*, 705−711.
(13) Breen, T. L.; Tien, J.; Oliver, S. R. J.; Hadzic, T.; Whitesides, G. M. Design and Self-Assembly of Open, Regular, 3D Mesostructures. *Science* **1999**, *284*, 948−951.
(14) Rapaport, D. C. Self-Assembly of Polyhedral Shells: A Molecular Dynamics Study. *Phys. Rev. E* **2004**, *70*, No. 051905.
(15) Rapaport, D. C. Role of Reversibility in Viral Capsid Growth: A Paradigm for Self-Assembly. *Phys. Rev. Lett.* **2008**, *101*, No. 186101.
(16) Boles, M. A.; Talapin, D. V. Self-Assembly of Tetrahedral CdSe Nanocrystals: Effective "Patchiness" via Anisotropic Steric Interaction. *J. Am. Chem. Soc.* **2014**, *136*, 5868−5871.
(17) Boles, M. A.; Engel, M.; Talapin, D. V. Self-Assembly of Colloidal Nanocrystals: From Intricate Structures to Functional Materials. *Chem. Rev.* **2016**, *116*, 11220−11289.
(18) Henzie, J.; Grünwald, M.; Cooper, A. W.; Geissler, P. L.; Yang, P. Self-Assembly of Uniform Polyhedral Silver Nanocrystals into Densest Packings and Exotic Superlattices. *Nat. Mater.* **2011**, *11*, 131−137.
(19) Damasceno, P. F.; Engel, M.; Glotzer, S. C. Predictive Self-Assembly of Polyhedra into Complex Structures. *Science* **2012**, *337*, 453−457.
(20) Cadotte, A. T.; Dshemuchadse, J.; Damasceno, P. F.; Newman, R. S.; Glotzer, S. C. Self-Assembly of a Space-Tessellating Structure in

the Binary System of Hard Tetrahedra and Octahedra. *Soft Matter* **2016**, *12*, 7073−7078.
(21) Pandey, S.; Ewing, M.; Kunas, A.; Nguyen, N.; Gracias, D. H.; Menon, G. Algorithmic Design of Self-Folding Polyhedra. *Proc. Natl. Acad. Sci. U.S.A.* **2011**, *108*, 19885−19890.
(22) Shigetomi, K. K.; Onoe, H.; Takeuchi, S. Cell Origami: Self-Folding of Three-Dimensional Cell-Laden Microstructures Driven by Cell Traction Force. *PLoS One* **2012**, *7*, No. e51085.
(23) Kaplan, R.; Klobušický, J.; Pandey, S.; Gracias, D. H.; Menon, G. Building Polyhedra by Self-Assembly: Theory and Experiment. *Artificial Life* **2014**, *20*, 409−439.
(24) Janbaz, S.; Noordzij, N.; Widyaratih, D. S.; Hagen, C. W.; Apachitei, L. E. F.; Zadpoor, A. A. Origami Lattices with Free-Form Surface Ornaments. *Sci. Adv.* **2017**, *3*, No. eaao1595.
(25) Ke, Y.; Ong, L. L.; Shih, W. M.; Yin, P. Three-Dimensional Structures Self-Assembled from DNA Bricks. *Science* **2012**, *338*, 1177−1183.
(26) Reinhardt, A.; Frenkel, D. Numerical Evidence for Nucleated Self-Assembly of DNA Brick Structures. *Phys. Rev. Lett.* **2014**, *112*, No. 238103.
(27) Douglas, S. M.; Dietz, H.; Liedl, T.; Hogberg, B.; Graf, F.; Shih, W. M. Self-Assembly of DNA into Nanoscale Three-Dimensional Shapes. *Nature* **2009**, *459*, 414−418.
(28) Aldaye, F. A.; Palmer, A. L.; Sleiman, H. F. Assembling Materials with DNA as the Guide. *Science* **2008**, *321*, 1795−1799.
(29) Mirkin, C. A.; Letsinger, R. L.; Mucic, R. C.; Storhoff, J. J. A DNA-Based Method for Rationally Assembling Nanoparticles into Macroscopic Materials. *Nature* **1996**, *382*, 607−609.
(30) Valignat, M. P.; Theodoly, O.; Crocker, J. C.; Russel, W. B.; Chaikin, P. M. Reversible Self-Assembly and Directed Assembly of DNA-Linked Micrometer-Sized Colloids. *Proc. Natl. Acad. Sci. U. S. A.* **2005**, *102*, 4225−4229.
(31) Nykypanchuk, D.; Maye, M. M.; van der Lelie, D.; Gang, O. DNA-Guided Crystallization of Colloidal Nanoparticles. *Nature* **2008**, *451*, 549−552.
(32) Liu, W.; Tagawa, M.; Xin, H. L.; Wang, T.; Emamy, H.; Li, H.; Yager, K. G.; Starr, F. W.; Tkachenko, A. V.; Gang, O. Diamond Family of Nanoparticle Superlattices. *Science* **2016**, *6273*, 582−586.
(33) Chen, G.; Gibson, K. J.; Liu, D.; Rees, H. C.; Lee, J.-H.; Xia, W.; Lin, R.; Xin, H. L.; Gang, O.; Weizmann, Y. Regioselective Surface Encoding of Nanoparticles for Programmable Self-Assembly. *Nat. Mater.* **2019**, *18*, 169−174.
(34) Sigl, C.; Willner, E.; Engelen, W.; Kretzmann, J.; Sachenbacher, K.; Liedl, A.; Kolbe, F.; Wilsch, F.; Aghvami, S.; Protzer, U.; Hagan, M.; Fraden, S.; Dietz, H. Programmable icosahedral shell system for virus trapping. *Nat. Mater.* **2021**, *20*, 1281−1289.
(35) Hayakawa, D.; Videbaek, T. E.; Hall, D. M.; Fang, H.; Sigl, C.; Feigl, E.; Dietz, H.; Fraden, S.; Hagan, M. F.; Grason, G. M.; Rogers, W. B. Geometrically programmed self-limited assembly of tubules using DNA origami colloids. *Proc. Natl. Acad. Sci. U.S.A.* **2022**, *119*, No. e2207902119.
(36) Tyukodi, B.; Mohajerani, F.; Hall, D. M.; Grason, G. M.; Hagan, M. F. Thermodynamic Size Control in Curvature-Frustrated Tubules: Self-Limitation with Open Boundaries. *ACS Nano* **2022**, *16*, 9077−9085.
(37) Xu, X.; Rosi, N. L.; Wang, Y.; Huo, F.; Mirkin, C. A. Asymmetric Functionalization of Gold Nanoparticles with Oligonucleotides. *J. Am. Chem. Soc.* **2006**, *128*, 9286−9287.
(38) Liu, W.; Halverson, J.; Tian, Y.; Tkachenko, A. V.; Gang, O. Self-organized architectures from assorted DNA-framed nanoparticles. *Nat. Chem.* **2016**, *8*, 867−873.
(39) Coxeter, H. S. M. Regular Skew Polyhedra in Three and Four Dimensions and their Topological Analogues. *Proc. London Math. Soc.* **1937**, *43*, 33−62.
(40) McMullen, P.; Schulte, E. *Abstract Regular Polytopes*; Cambridge University Press: Cambridge, 2002.
(41) Hyde, S.; Blum, Z.; Landh, T.; Lidin, S.; Ninham, B. W.; Andersson, S.; Larsson, K. *The Language of Shape*; Elsevier: Amsterdam, 1997.
(42) Hyde, S. T.; O'Keeffe, M. O.; Proserpio, D. M. A Short History of an Elusive Yet Ubiquitous Structure in Chemistry, Materials, and Mathematics. *Angew. Chem., Int. Ed. Engl.* **2008**, *47*, 7996−8000.
(43) Schoen, A. H. Infinite Periodic Minimal Surfaces without Self-Intersections; *Technical Note NASA-TN-D-5541*; National Aeronautics and Space Administration: Washington, DC, 1970; https://ntrs.nasa.gov/citations/19700020472 (accessed 2022−11−23).
(44) Dotera, T. Tricontinuous Cubic Structures in ABC/A/C Copolymer and Homopolymer Blends. *Phys. Rev. Lett.* **2002**, *89*, No. 205502.
(45) Robins, V.; Ramsden, S. J.; Hyde, S. T. 2D Hyperbolic Groups Induce Triply-Periodic Euclidean Reticulations. *Euro. Phys. J. B* **2004**, *39*, 365−375.
(46) Dotera, T.; Tanaka, H.; Takahashi, Y. Hexagulation Numbers: The Magic Numbers of Equal Spheres on Triply Periodic Minimal Surfaces. *Struct. Chem.* **2017**, *28*, 105−112.
(47) Wilts, B. D.; Zubiri, B. A.; Klatt, M. A.; Butz, B.; Fischer, M. G.; Kelly, S. T.; Spiecker, E.; Steiner, U.; Schröder-Turk, G. E. Butterfly Gyroid Nanostructures as a Time-Frozen Glimpse of Intracellular Membrane Development. *Sci. Adv.* **2017**, *3*, No. e1603119.
(48) Pedersen, M. C.; Hyde, S. T. Polyhedra and Packings from Hyperbolic Honeycombs. *Proc. Natl. Acad. Sci. U.S.A.* **2018**, *115*, 6905−6910.
(49) Reddy, A.; Dimitriyev, M. S.; Grason, G. M. Medial Packing and Elastic Asymmetry Stabilize the Double-Gyroid in Block Copolymers. *Nat. Commun.* **2022**, *13*, 2629.
(50) Hart, G. W. Gyrangle *Web Page*. https://www.georgehart.com/DC/ (accessed 2022−11−23).
(51) Sarhangi, R. The Story of Gyrangle. *Notices of the AMS* **2011**, *58*, 690−692.
(52) Wells, A. F. *Three-Dimensional Nets and Polyhedra*; John Wiley & Sons: New York, 1977.
(53) Steinhardt, P. J.; Nelson, D. R.; Ronchetti, M. Bond-Orientational Order in Liquids and Glasses. *Phys. Rev. B* **1983**, *28*, 784−805.

https://doi.org/10.1021/acsnano.2c11929
ACS Nano 2023, 17, 15371−15378